Dynamics of double-pulse laser printing of copper microstructures

Qingfeng Li, David Grojo, Anne-Patricia Alloncle, Philippe Delaporte

Contents lists available at ScienceDirect

Applied Surface Science

journal homepage: www.elsevier.com

Full Length Article

Dynamics of double-pulse laser printing of copper microstructures

Qingfeng Li*, David Grojo, Anne-Patricia Alloncle, Philippe Delaporte

Aix-Marseille University, CNRS, LP3 Laboratory, Campus de Luminy, 13009 Marseille, France

ARTICLE INFO

Keywords:
Double pulse
Laser-induced forward transfer
Microstructure printing
Copper

ABSTRACT

Laser induced forward transfer process can be implemented in a double-pulse scheme where a solid thin film deposited on a transparent donor substrate is irradiated by two synchronized lasers. In a recently demonstrated methodology, a long pulse is first applied to melt the film and an appropriately delayed ultrashort laser pulse initiates material transfer in the liquid phase toward a receiver substrate. This provides a versatile method to print high-resolution (< 2 μm) patterns with a long working distance (> 40 μm). In this paper we focus on the study of the dynamical aspects associated with these printing performances. The temperature evolution of the thin copper film during irradiation with a quasi-continuous wave (QCW) pulse is calculated. By combining the calculations with time-resolved imaging experiments, we reveal the influence of the copper film temperature and molten metal diameter on the ejection dynamics. Characterization of the transferred materials shows that the delay between the two laser pulses is a control parameter for the shape and volume of the printed structures. This is finally exploited to demonstrate high-precision printing of different debris-free microstructures onto a Si receiver substrate set as far as 60 μm away from the donor film.

1. Introduction

Recently, the double-pulse laser-induced forward transfer (DP-LIFT) process has been successfully applied for generating liquid nano-jets from solid donor films and consequently transfer various materials (Cu, Au, Ag, Ni) on a receiving substrate with well-defined and debris-free depositions [1,2]. However, due to the numerous mechanisms taking place during the double-pulse process, the physics behind this novel laser-induced jetting and deposition technique is not fully understood yet. LIFT related jetting phenomenon from low viscosity liquid donors has been extensively investigated by several groups, both experimentally [3–6] and numerically [7–9]. These studies point out that the jetting mechanism is initiated by an expanding cavitation bubble generated between the donor substrate and the liquid-free surface. However, in the DP-LIFT situation, the typical thickness of the donor film is below 1000 nm, and thus, such a cavitation bubble driving mechanism would require a strong downscaling of the bubble size and make it unlikely. Besides, laser-induced nano-jetting from ultra-thin (< 100 nm) solid donor films has been reported and investigated experimentally [10–16] and theoretically [17–19]. In these experiments, an ultrashort pulse irradiates the thin film with a Gaussian beam profile which induces a Gaussian distributed pressure force in a film melted over its full thickness in the irradiated area. Under appropriate conditions, the molten film can detach from the substrate with the shape of a dome shell. Within this dome shell the normal component of the capillary force decelerates the normal velocity of the shell and the parallel component leads to the displacement of the shell material towards the center. Taken these effects all together, a jet starts to form when the reverse motion of the shell begins [17]. A difference with the DP-LIFT situation is the diameter of the melted area which is only 1 to 2 orders of magnitude larger than the dimension of the ultrafast laser spot used in these experiments. The much larger melted area achieved in DP-LIFT, makes less relevant the above-mentioned description based on a locally detached dome shell for this process, and such a dome has never been observed in this configuration. For these reasons, the dynamical aspect associated to DP-LIFT remains unclear and requires further investigations. Looking at the already performed DP-LIFT experiments [1,2,20,21], even though they have demonstrated the unique features and liquid metal jetting behaviors, they have not been dedicated to study the specificities of the laser printing in this configuration. By comparing the calculated time-evolution of the film temperature initiated with the pre-pulse and the experimental observations of both the ejection dynamics and the printed structures, we intend here to investigate these aspects to improve the physical understanding of nano-jetting. This allows also finding new parameters to finely control

* Corresponding author.
Email address: li@lp3.univ-mrs.fr (Q. Li)

https://doi.org/10.1016/j.apsusc.2018.12.052
Received 28 August 2018; Received in revised form 20 November 2018; Accepted 5 December 2018
Available online xxx

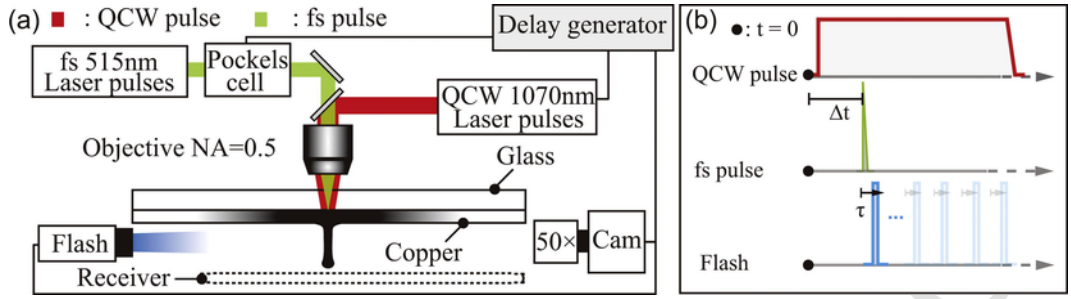

Fig. 1. (a) Sketch of the experimental setup for DP-LIFT. The femtosecond LIFT laser beam is represented in green and the QCW laser beam in red. Illumination flash light is shown by the blue color. (b) Time chart of events for synchronization of the DP-LIFT and time-resolved observations.

Table 1
Thermal and hydrodynamic parameters of copper for different temperatures.

Temperature [K]	Thermal conductivity [W m^{-1} K^{-1}]	Heat capacity [J kg^{-1} K^{-1}]	Density [kg m^{-3}]	Viscosity [mPas]	Surface tension [mN/m]
293	400	382	8960	–	–
573	381	413	8809	–	–
1400	167	516	7907	3.74	1280
1850	180	516	7576	2.14	1220

the shape and the volume of the printed structures, and subsequently optimize the performance of DP-LIFT for digital micro- nano-printing.

2. Materials and methods

2.1. Experimental setup

The experimental arrangement implemented to investigate various aspects of the DP-LIFT process is depicted in Fig. 1(a). The laser source used to achieve the melting of the donor film is a quasi-continuous wave (QCW) laser (IPG PHOTONICS YLR-150/1500-QCW-AC-Y14) emitting, at 1070-nm wavelength, pulses of variable duration from 50 µs to the continuous wave operation. Synchronized with the QCW laser irradiation, a femtosecond laser (AMPLITUDE SYSTEMES S-Pulse HP), delivers at 515 nm wavelength (second harmonic), pulses of 500 fs duration (FWHM) and focused at the center of the melted region to induce material ejections. Both beams enter collinearly through a long working distance 0.55NA (MITUTOYO M Plan Apo 50×) objective lens. The measured beam diameters at half maximums (FWHM) at the copper-donor interface are respectively 1.6 µm for the femtosecond laser and 9.7 µm for the QCW laser. The power of both lasers is independently adjusted using half-wave plate and polarizer combinations. The positioning of the two beams and the systematic inspection of the donor film is facilitated by a customized reflection microscopy arrangement (not shown here). Time-resolved shadowgraphs of material ejections are recorded using a CCD camera (QIMAGING QICAM) mounted on a customized microscopy arrangement based on a 50× super-long working distance microscope objective lens (MITUTOYO M Plan Apo SL NA = 0.4). Bright-field flash illumination is provided by a nanosecond flash lamp (HIGH-SPEED PHOTO-SYSTEME KL-M NANOLITE). The flash duration of 12 ns determines the temporal resolution of the acquisition system. A digital delay generator (STANFORD RESEARCH SYSTEMS DG645) is used to precisely synchronize, with adjustable delay, the two laser pulses and the flash lamp to perform time-resolved shadowgraphy imaging. As illustrated in Fig. 1(b), the delay Δt between the initial time (t = 0) of the sequence and the femtosecond laser pulse can be arbitrarily adjusted by the delay generator. For each sequence, the flash light will illuminate the field-of-interest with a preset flash-to-LIFT delay τ to acquire with the camera a snapshot of the ejection event occurring at a delay τ after the fs pulse. In this paper, conditions corresponding to different Δt delays and various τ are investigated. For all the experiments presented in this paper, a 1-µm thick copper film with a 25 nm chromium interlayer (magnetron sputtering onto a 1-mm-thick glass substrate) is used as donor film.

2.2. QCW heating model

In DP-LIFT, the role of the irradiation by the first QCW pulse is to induce a local melting on the donor film. At fixed QCW power, when the second femtosecond pulse irradiates the heated donor film with different delays Δt, the donor film exhibits different temperatures below or above melting. For copper, as shown in Table 1, some of the physical properties of the film are significantly temperature-dependent [22–25]. One can expect different behaviors depending on the hydrody-

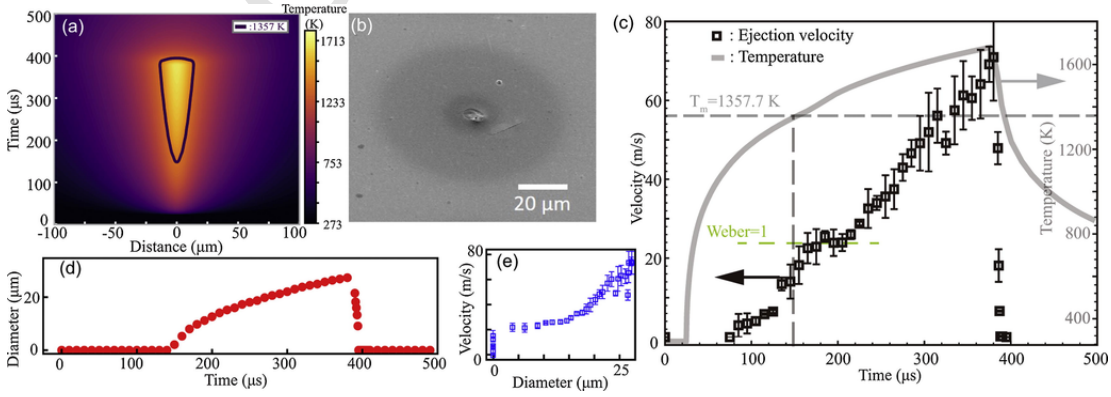

Fig. 2. Space-time characteristics of the copper film and ejections during the DP-LIFT process. (a) Time-evolution of the lateral temperature distribution of the donor copper film under QCW pulse irradiation. (b) SEM image of the film after the DP-LIFT process. (c) Time-evolution of the temperature evolution in the central region of the QCW beam and the measured ejection velocities as a function of LIFT time (synchronization of the fs pulse). The melting temperature of copper under atmospheric pressure is 1357.7 K and shown by a horizontal dash line on the graph. (d) Time-evolution of diameter of the molten film region. (e) Measured ejection velocities as a function of melting pool diameter.

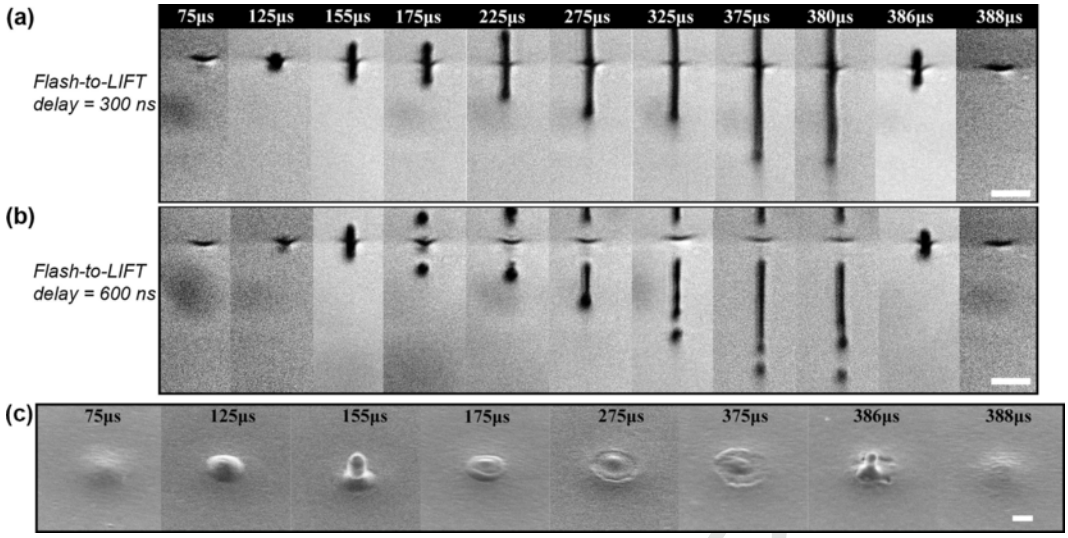

Fig. 3. Shadowgraphy images of ejections at different LIFT times during the QCW irradiation, with LIFT-to-flash delays of 300 ns (a) and 600 ns (b), scale bars: 10 μm. (c) SEM image of remaining structures on the donor film after the DP-LIFT process at different LIFT times, scale bar: 2 μm.

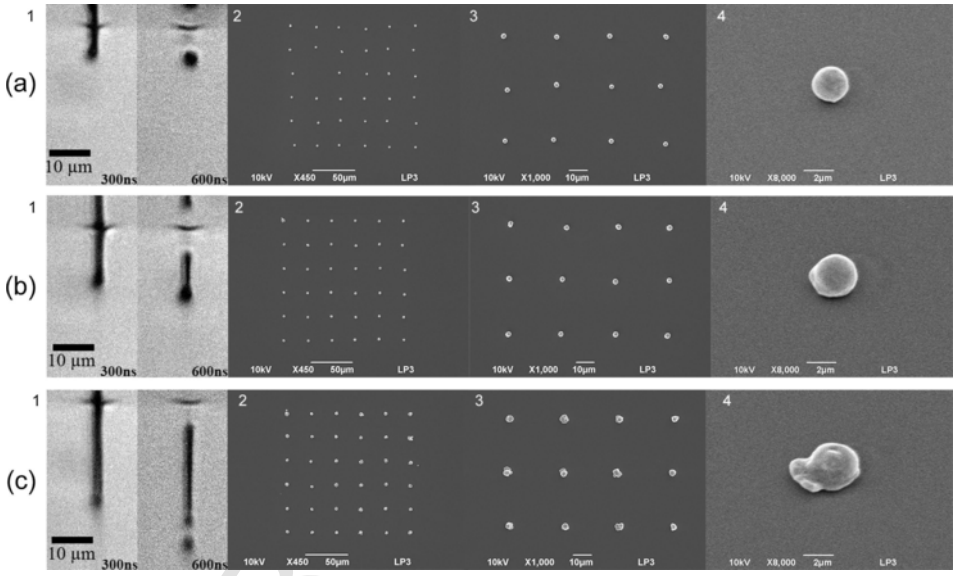

Fig. 4. Ejection induced by DP-LIFT process and the printed pixel matrixes with QCW-to-fs delays of 195 μs (a); 275 μs (b) and 375 μs (c). In column 1, we present the ejection images corresponding to each condition. By placing a silicon receiver at 50 μm in front of the donor and performing DP-LIFT process with different QCW-to-fs delays, column 2, 3 and 4 show the printed results at different observation magnifications.

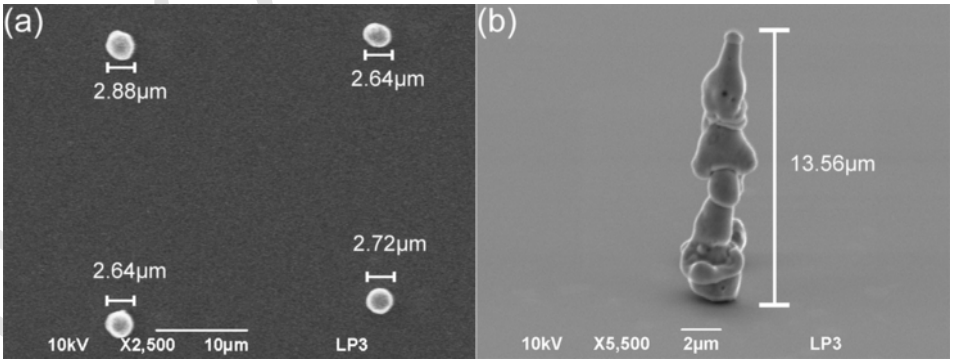

Fig. 5. By placing a silicon receiver at 50- μm distance in front of the donor and repeated DP-LIFT processes with a QCW-to-fs delay of 275 μs, a 2.5D microstructures are formed. (a) Array of four individual droplets separated by an interval of 30 μm. (b) A micro-column formed by four droplets stacked on top of each other.

namic characteristics of the film such as the dynamic viscosity and the surface tension. Accordingly, it is worth investigating the ejection dynamics of liquid copper for different temperatures simply controlled by varying the delay between the two laser pulses. For the interpretation, the impact of the molten pool diameter (also varying) should also be taken into account as it will have an influence on the pressure distribution in the liquid film, which is known to play a key role in some ejection processes. For this reason, the space-time evolution of the film temperature under irradiation by the QCW pulse irradiation is first calculated.

The heating process of the donor by the QCW pulse is governed by the general heat equation:

$$\rho C_p \frac{\partial T}{\partial t} - \nabla (k \nabla T) = Q \tag{1}$$

which gives the temperature T in the system in response to a heat source Q. The enthalpies of fusion and vaporization are incorporated by adding a Gaussian function to the heat capacity C_p, centered at the equilibrium phase-change temperatures, exhibiting a width of 20 K. The density ρ and thermal conductivity k are temperature dependent [26,27]. Thus, the heat equation which describes this process is numerically solved. The heat source Q corresponds to the absorption of the QCW laser energy, with a Gaussian profile along x direction, parallel to the film surface. According to the Beer-Lambert law and taking into account multiple internal reflections in the thin film the heat source is expressed as

$$Q = I_0(t)\,\alpha\,(1 - R)\,exp\left(\frac{-2x^2}{\omega_0^2}\right) exp\left(\frac{exp(-\alpha z)}{1 - exp(-\alpha D)}\right), \tag{2}$$

where R represents the reflection coefficient, α the linear absorption coefficient, D the thickness of the thin film, ω_0 the beam waist and z the absorption direction. For all the experiments presented in this article, the QCW laser and the sequence is driven by an electrical square pulse of 400-μs duration. Its raising edge defines the initial time (t = 0 μs). The optical output power of the QCW laser pulse starts at t = 24 μs and is constant until it exponentially decays at t = 383 μs (see Fig. 1b), reaching zero at t = 400 μs. To fulfill the actual temporal evolution of the optical output, the QCW laser puls e intensity $I_0(t)$ is described by a piecewise function:

$$I_0(t) = \begin{cases} 0 : 0 \le t < 24\ \mu s \\ \frac{2E_P}{\pi\omega_0^2\tau_{qcw}} : 24 \le t < 383\ \mu s \\ \frac{2E_P}{\pi\omega_0^2\tau_{qcw}} exp\left(-\frac{(t-383)^2}{40}\right) : 383 \le t < 400\ \mu s \\ 0 : t \ge 400\ \mu s \end{cases} \tag{3}$$

where E_p is the QCW pulse energy measured as 770 μJ ± 70 μJ in the experiments and τ_{qcw} is the total pulse duration measured as 378 μs (from t = 24 μs to t = 400 μs).

3. Results and discussion

3.1. Ejections at different Cu temperatures

Using numerical simulations, the temperature evolution of the donor film under QCW pulse irradiation is calculated from t = 0 μs to t = 500 μs and presented in Fig. 2. More precisely, the time-evolution of the lateral temperature distribution is mapped out and shown in Fig. 2(a). The donor film thickness is small enough (1-μm) to consider the temperature to be uniform in the z-direction (whole thickness). The solid line plot on this graph shows the contour line for the melted region (temperature above the fusion point). To have an overview of the heat affected area after DP-LIFT, a SEM image of the corresponding processed area on the donor film is presented in Fig. 2(b). A light grey disk with diameter of ≈60 μm refers to the heat affected zone after the QCW laser irradiation and a dark grey disk with diameter ≈20 μm refers to the re-solidified material after melting. At the center of the molten pool, a vestige of surface pinching can be observed. This observation proves that a jet is initiated at the center of the QCW laser spot. As this central region also corresponds to the maximum temperature of the donor film, we plot its temporal evolution in Fig. 2(c). Referring to the temporal profile of the QCW pulse described in Eq. (2), the copper film temperature starts to rise at t = 24 μs and the central region reaches the melting point at t = 150 μs. From Fig. 2(c), we can see that the temperature raises up to its highest value of 1689 K at t = 383 μs before to drop sharply at t = 395 μs leading to the re-solidification of the film. In Fig. 2(d), the time-evolution of the molten pool diameter during this process is also presented. A similar evolution can be observed for this parameter. The molten pool starts to form at t = 150 μs and the maximum diameter 27.4 μm is reached at t = 383 μs. After that, the molten pool diameter decreases sharply and at t = 395 μs the molten pool has completely disappeared.

With the knowledge of the temperature of the copper donor film under the QCW pulse irradiation and the experimental observations of the ejection dynamics using the setup presented in Fig. 1, it becomes possible to investigate the impact of different molten pool temperatures and diameters on the ejection behaviors. We have performed DP-LIFT experiments for different QCW-to-fs delays Δt (see Fig. 1(b)) without the presence of a receiver substrate. As shown in Fig. 3, the time-resolved observations of the ejection events are captured with LIFT-to-flash delays τ of 300 nsand 600 ns.

During the heating process, the femtosecond LIFT laser with the pulse energy of 2 μJ irradiates the middle of the heated zone with delay Δt with respect to the experimental initial moment (t = 0). The LIFT-to-flash delay τ was first set at 300 ns in order to illuminate the ejection before any droplet develops. As shown in Fig. 3(a), jetting seems to appear at Δt = 125 μs From Δt = 175 μsto 380 μs the length of the jet increases, because of higher ejection velocities, and then diminished rapidly until no significant jetting is observed after Δt = 388 μs. The second LIFT-to-flash delay τ was set at 600 ns in order to observe the ejection after the potential appearance of droplets. First, the shadowgraphy images acquired for this delay show that there is no evolution of the copper film motion between τ = 300 ns and τ = 600 ns for Δt delays shorter 155 μs or longer than 385 μs. There is no ejection occurring for these conditions. Even if a jet seems to be initiated at Δt = 155 μsand Δt = 386 μsone should note that it cannot escape from the donor surface. From Δt = 175 μs to 380 μs jets encounter different pinch-off processes and evolve into equilibrium spheres, complex oscillators or the so-called endpinching depending on the initial aspect ratio of the jets. It is interesting to mention that these observations are consistent with the theoretical prediction of Notz et al. [28], even though the jet radius is downscaled down to the micrometer scale in our experiments. To help in the interpretation of these mechanisms, the morphologies of the donor film surface after the DP-LIFT process are also presented in Fig. 3(c) for each experimental condition. By using the shadowgraphy images acquired at the two times, we have also calculated the average velocity of the ejection. This average velocity is plotted in the graph of Fig. 2(c) to highlight the correlation with temperature evolution of the donor film.

According to these investigations, a first conclusion is that the impact of the copper film temperature on the process does not lead to a binary response associated with melted or unmelted films. This parameter plays a significant role in the dynamics of the laser-induced jetting process. When the donor film is melted, as the temperature increases, the initial ejection velocity increases. As both optical (reflectivity) and hydrodynamics (surface tension and viscosity) parameters are temperature related, we have tried first to correlate the temperature evolution to the ejection velocity changes using an energy balance model treatment (see supplementary materials). However, the velocity

variations that can be predicted by this approach are not as large as those observed in our experiments and plotted in Fig. 2(c). This is most probably caused by the influence of the molten pool size ignored in our calculations. To establish the correlation between the molten pool diameter and the ejection velocity, we plot in Fig. 2(e) the measured ejection velocities as a function of calculated molten pool diameters. From 15 μm to 25 μm the ejection velocities are proportional to the molten pool diameters. This is of significant technical importance as the time–evolution of the molten pool diameter during the DP-LIFT process allows us to access in principle a wide range of ejection regimes without changing neither the laser parameters (energy, fluence, pulse duration, etc.) nor the donor thickness.

3.2. Ejection regimes

3.2.1. Bump-like deformations

With the space-time evolution of the film temperature provided in Fig. 2, we determined that in DP-LIFT configuration with femtosecond LIFT pulse arriving with delay $\Delta t = 75\,\mu s$, the temperature of the donor film is high (>1100 K at QCW spot center) but still remains in its solid phase. Accordingly, as shown in Fig. 3(c) (75 μs), there is no flow motion occurring at the free surface and finally the femtosecond pulse induces a pressure simply leading to a bump-like deformation of the donor film. At continuously increasing delays up to $\Delta t = 125\,\mu s$ the temperature reaching about 1300 K near the melting point. For this condition, it can be seen in Fig. 3 that the femtosecond LIFT pulse produces a local expansion that can be observed at the early time ($\tau = 300$ ns) whereas this motion will be quickly stopped before $\tau = 600$ ns. This will finally lead to a bump-like deformation with a higher aspect ratio on the donor film as shown in Fig. 3(c) (125 μs).

3.2.2. Dynamics below ejection threshold

As the donor temperature continuously increases with delay above 125 μs, local melting of the film starts to occur, and the liquid motion induced by the femtosecond pulse irradiation changes drastically the dynamical response of the film. It can be observed that from $\Delta t = 125$ μs to $\Delta t = 155\,\mu s$ the deformation velocity jumps from 7.4 ± 0.5 m/s to 22.2 ± 3.3 m/s. This is due to conditions for which the temperature of the copper film crosses the melting point (from 1303 K to 1368 K). For the same conditions, the molten pool diameter increases from 0 to 3.8 μm.

However, Figs. 2(c) and Fig. 3(a-b) show that, from $\Delta t = 155\,\mu s$ to 165 μs (see Fig. s1), even if the copper is molten and liquid ejection initially appears, the material does not escape from the free surface. The SEM image shown in Fig. 3(c) (155 μs) also confirms this behavior. In fact, this trapping can be explained by comparing the values of the kinetic energy and the surface energy, as the ejection can only occur if the kinetic energy of the expelled material exceeds the surface energy [7,29]. The dimensionless Weber number We_{ej} can be used to characterize this relation. It is given by the ratio:

$$\frac{E_{kin}}{E_s} \approx \frac{\rho(T)\, d_l V_{ej}^2}{2\gamma(T)} = We_{ej}. \tag{4}$$

The material escape threshold condition corresponds to $We_{ej} = 1$ and that allows the calculation of a minimal required velocity V_{ej_min} found at 24 $m/s$and matching remarkably well with the measured velocity at $\Delta t = 175\,\mu s$(see Fig. 2(c)).

3.2.3. Dynamics above escape threshold

From $\Delta t = 175\,\mu s$ to $\Delta t = 380\,\mu s$ the average ejection velocity increases from 23.4 ± 2.3 m/s to 74.5 ± 3.4 m/s with a temperature increase from T = 1411 K to 1689 K and a molten pool diameter increase from 8.8 μm to 27.4 μm. It is worth to notice that, under those conditions, the average ejection velocity is proportional to the molten pool diameters. From SEM images presented in Fig. 3(c) one can also observe that there is no significant protrusion structures formed on the surface for these conditions. Only some ripples are observed. Shadowgraphy observations presented in Fig. 3(b) show that, the DP-LIFT generated jets pinch off at the surface for these conditions. Interestingly, these surface pinching and protrusion free features are different from most of the reported laser-induced nano-jetting phenomenon generated from ultra-thin metal films [10–16]. In those cases, the jetting process involved with the competition between inertia-capillary dynamics and crystallization, in which the jet elongates and breaks up into droplets due to the Plateau-Rayleigh instability and the formation of a neck occurs in the solidification zone between the crystalline and liquid parts of the jet [17].

3.3. Printed copper microstructures

3.3.1. Droplet arrays printed with different QCW-to-fs delays

According to the previous discussions, the ejection behavior depends on the QCW-to-fs delay. A direct benefit from this finding is that it allows us to perform pixel-to-pixel printing with controllable pixel shapes and sizes. By placing a silicon receiver substrate at 50 μs distance in front of the donor film, the ejected material can be readily collected. Then, by repeating the DP-LIFT process and controlling the motion of the receiver and donor substrates, 2D patterns with arbitrary designs can be printed on the receiver. As a first demonstration, we have printed three 6 × 6 matrices with a period of 30 μm for three different QCW-to-fs delays.

As shown in Fig. 4(a1), for a QCW-to-fs delay $\Delta t = 195\,\mu s$, the ejection of the liquid copper have evolved into an equilibrium sphere at $\tau = 600$ ns after a travel distance of 8 μm. The corresponding average flying velocity is $V_f \cong 13$ m/s. Under this condition, due to the low initial aspect ratio, the droplet will keep its spherical shape once the equilibrium is established. Due to the short transfer distance of 50 μm, the air drag effect can be neglected and one can assume that the impact velocity on the receiver is directly $V_{im} = V_f$. When the droplet reaches the receiver, its diameter d is 2.5 μm and the impact Weber number We_{im} can be approximated as:

$$We_{im} = \frac{\rho d V_{im}^2}{\gamma} = 2.6. \tag{5}$$

Thus, as presented in Fig. 4(a4), when the droplet wets the receiver with such a small Weber number it can hardly spread and finally solidifies with a sphere [30]. In Fig. 4(a2) and (a3), the repeatability is demonstrated by the matrix printing. The average diameter of the printed droplets is measured as 2.40 μm with a deviation of ± 0.23 μm.

For $\Delta t = 275\,\mu s$, as shown in Fig. 4(b1), the material is ejected as a jet which has travelled a distance of 18 μm at $\tau = 600$ ns. When this ejection reaches the receiver, the impact Weber number We_{im} is approximately 13.7. Under these conditions, as presented in Fig. 4(b4), the printed droplet starts to spread on the receiver. Compared to the previous case, and the droplets exhibit discontinuities at the surface and contours. This feature indicates that the pinch-off of the jet must have started before the material reaches the receiver and the re-solidification stage. The consequence is that the quality of the printed pixels suffers from the merging of segmented droplets. In Fig. 4(b2) and (b3), a printed pixel matrix under these conditions is shown. The average diameter of the printed droplets is measured as 2.77 μm with a deviation of ± 0.12 μm. This corresponds to a feature size larger than the one of the previous case but with a similar repeatability.

For $\Delta t = 375\,\mu s$, as shown in Fig. 4(c1), this long liquid jet starts to pinch-off followed by a so-called endpinching mechanism at $\tau = 600$ ns for a travel distance of 36 μm. When the ejected material reaches the receiver the impact Weber number We_{im} is approximately 54.8. As presented in Fig. 4(c4), similarly to previous case, the corresponding printed droplets exhibit rough contours and discontinuities, but they

are also somehow squeezed with a flatten shape. In Fig. 4(c2) and (c3), a printed pixel matrix is also shown, and the average diameter of the printed droplets is measured as 4.22 μm with a deviation of ± 0.48 μm.

3.3.2. High-aspect ratio copper microstructures

As presented in the last section, it is for the conditions with $\Delta t = 275\,\mu s$ that the printed droplets exhibit the best reproducibility. For this reason, we have chosen these printing conditions to demonstrate the ability of building microstructures in the third dimension by repeated DP-LIFT technique at the same location. In Fig. 5(b), we show the structure obtained after printing four droplets while the receiver is kept at the same location. The droplets are piled one by one on top of each other to finally form a micro-column with a height of 13.6 μm without any debris around the structure. Despite the drawback of the inherent discontinuity of the structures formed by this mean, the ability to assemble droplets in the third dimension represents a critical step for technological considerations.

4. Conclusions

In conclusion, we have demonstrated laser-induced jetting from a copper film of 1-μm thickness using a dual laser approach and the associated ejection dynamics were investigated. The space-time temperature evolution of the donor film under illumination has been numerically calculated. By irradiating the heated film with identical femtosecond pulses at different delays, we have observed different ejection regimes. By comparison between the thermal simulations and time-resolved imaging of the material ejections, we conclude that the size of the melted region more than the copper film temperature plays an essential role in the jetting ejection dynamics. A technological benefit of these results is the possibility to achieve multi-scale printing without changing neither the laser parameters (energy, fluence, pulse duration, etc.) nor the donor thickness. Droplet matrices with pixel diameters from 2.40 ± 0.23 μm to 4.22 ± 0.48 μm and micro-column with a height of 13.6 μm are successfully printed without any debris. This shows the potential of this DP-LIFT approach for the development of a true−3D laser nano- micro-printing technology.

Appendix A. Supplementary material

Supplementary data to this article can be found online at https://doi.org/10.1016/j.apsusc.2018.12.052.

References

[1] Q. Li, A.P. Alloncle, D. Grojo, P. Delaporte, Generating liquid nanojets from copper by dual laser irradiation for ultra-high resolution printing, Opt. Exp. 25 (2017) 24164, https://doi.org/10.1364/OE.25.024164.

[2] Q. Li, A.P. Alloncle, D. Grojo, P. Delaporte, Laser-induced nano-jetting behaviors of liquid metals, Appl. Phys. A Mater. Sci. Process. 123 (2017) https://doi.org/10.1007/s00339-017-1308-4.

[3] M. Duocastella, J.M. Fernández-Pradas, J.L. Morenza, P. Serra, Time-resolved imaging of the laser forward transfer of liquids, J. Appl. Phys. 106 (2009) 084907, https://doi.org/10.1063/1.3248304.

[4] C. Boutopoulos, I. Kalpyris, E. Serpetzoglou, I. Zergioti, Laser-induced forward transfer of silver nanoparticle ink: time-resolved imaging of the jetting dynamics and correlation with the printing quality, Microfluid. Nanofluidics. 16 (2014) 493–500, https://doi.org/10.1007/s10404-013-1248-z.

[5] C. Unger, M. Gruene, L. Koch, J. Koch, B.N. Chichkov, Time-resolved imaging of hydrogel printing via laser-induced forward transfer, Appl. Phys. A Mater. Sci. Process. 103 (2011) 271–277, https://doi.org/10.1007/s00339-010-6030-4.

[6] E. Biver, L. Rapp, A.-P. Alloncle, P. Serra, P. Delaporte, High-speed multi-jets printing using laser forward transfer: time-resolved study of the ejection dynamics, Opt. Exp. 22 (2014) 17122–17134, https://doi.org/10.1364/OE.22.017122.

[7] M.S. Brown, C.F. Brasz, Y. Ventikos, C.B. Arnold, Impulsively actuated jets from thin liquid films for high-resolution printing applications, J. Fluid Mech. 709 (2012) 341–370, https://doi.org/10.1017/jfm.2012.337.

[8] E. Bourasseau, A. Homman, O. Durand, A. Ghoufi, P. Malfreyt, Calculation of the surface tension of liquid copper from atomistic Monte Carlo simulations To cite this version: calculation of the surface tension of liquid copper from atomistic Monte Carlo simulations, Eur. Phys. J. B Condens. Matter Complex Syst. 86 (2013) 251.

[9] A. Pearson, E. Cox, J.R.R. Blake, S.R.R. Otto, Bubble interactions near a free surface, Eng. Anal. Bound. Elem. 28 (2004) 295–313, https://doi.org/10.1016/S0955-7997(03)00079-1.

[10] Y. Nakata, N. Miyanaga, K. Momoo, T. Hiromoto, Solid-liquid-solid process for forming free-standing gold nanowhisker superlattice by interfering femtosecond laser irradiation, Appl. Surf. Sci. 274 (2013) 27–32, https://doi.org/10.1016/j.apsusc.2013.02.042.

[11] U. Zywietz, C. Reinhardt, A.B. Evlyukhin, T. Birr, B.N. Chichkov, Generation and patterning of Si nanoparticles by femtosecond laser pulses, Appl. Phys. A Mater. Sci. Process. 114 (2014) 45–50, https://doi.org/10.1007/s00339-013-8007-6.

[12] F. Korte, J. Koch, B.N. Chichkov, Formation of microbumps and nanojets on gold targets by femtosecond laser pulses, Appl. Phys. A. 79 (2004) 879–881, https://doi.org/10.1007/s00339-004-2590-5.

[13] J.P. Moening, S.S. Thanawala, D.G. Georgiev, Formation of high-aspect-ratio protrusions on gold films by localized pulsed laser irradiation, Appl. Phys. A Mater. Sci. Process. 95 (2009) 635–638, https://doi.org/10.1007/s00339-009-5166-6.

[14] C. Unger, J. Koch, L. Overmeyer, B.N. Chichkov, Time-resolved studies of femtosecond-laser induced melt dynamics, Opt. Exp. 20 (2012) 24864–24872, https://doi.org/10.1364/OE.20.024864.

[15] A.A. Kuchmizhak, A.V. Nepomnyashchii, O.B. Vitrik, Y.N. Kulchin, Plasmon-mediated enhancement of rhodamine 6G spontaneous emission on laser-spalled nanotextures, Phys. Procedia. 86 (2017) 66–71, https://doi.org/10.1016/j.phpro.2017.01.023.

[16] D. Wortmann, J. Koch, M. Reininghaus, C. Unger, C. Hulverscheidt, D. Ivanov, B.N. Chichkov, Experimental and theoretical investigation on fs-laser-induced nanostructure formation on thin gold films, J. Laser Appl. 24 (2012) 042017, https://doi.org/10.2351/1.4734048.

[17] S.I. Anisimov, V.V. Zhakhovsky, N.A. Inogamov, S.A. Murzov, V.A. Khokhlov, Formation and crystallisation of a liquid jet in a film exposed to a tightly focused laser beam, Quant. Electron. 47 (2017) 509–521.

[18] N.A. Inogamov, V.V. Zhakhovsky, V.A. Khokhlov, Y.V. Petrov, K.P. Migdal, Solitary nanostructures produced by ultrashort laser pulse, Nanoscale Res. Lett. 11 (2016) 177, https://doi.org/10.1186/s11671-016-1381-1.

[19] N.A. Inogamov, V.V. Zhakhovskii, V.A. Khokhlov, Jet formation in spallation of metal film from substrate under action of femtosecond laser pulse, J. Exp. Theor. Phys. 120 (2015) 15–48, https://doi.org/10.1134/S1063776115010136.

[20] A. Narazaki, R. Kurosaki, T. Sato, Y. Kawaguchi, H. Niino, On-demand deposition of functional oxide microdots by double-pulse laser-induced dot transfer, J. Laser Micro Nanoeng. 9 (2014) 10–14, https://doi.org/10.2961/jlmn.2014.01.0003.

[21] A. Klini, P.A. Loukakos, D. Gray, A. Manousaki, C. Fotakis, Laser induced forward transfer of metals by temporally shaped femtosecond laser pulses, Opt. Exp. 16 (2008) 11300–11309, https://doi.org/10.1364/OE.16.011300.

[22] L. Battezzati, A.L. Greer, The viscosity of liquid metals and alloys, Acta Metall. 37 (1989) 1791–1802, https://doi.org/10.1016/0001-6160(89)90064-3.

[23] I. Egry, G. Lohoefer, G. Jacobs, Surface tension of liquid metals: results from measurements on ground and in space, Phys. Rev. Lett. 75 (1995) 4043–4046, https://doi.org/10.1103/PhysRevLett. 75.4043.

[24] Y. Baba, T. Inoue, K. Sugioka, H. Kobatake, H. Fukuyama, M. Kubo, T. Tsukada, Thermal conductivity measurement of molten copper using an electromagnetic levitator superimposed with a static magnetic field, Meas. Sci. Technol. 23 (2012) 045103, https://doi.org/10.1088/0957-0233/23/4/045103.

[25] J.J. Valencia, P.N. Quested, Thermophysical Properties, ASM Hadbook, vol. 15, Cast. 15, 2011, pp. 468–481. https://doi.org//10.1361/asmhba0005240.

[26] M.J. Assael, A.E. Kalyva, K.D. Antoniadis, R. Michael Banish, I. Egry, J. Wu, E. Kaschnitz, W.A. Wakeham, Reference data for the density and viscosity of liquid copper and liquid tin, J. Phys. Chem. Ref. Data. 39 (2010) 1–8, https://doi.org/10.1063/1.3467496.

[27] C. Cagran, Thermal Conductivity and Thermal Diffusivity of Liquid Copper, Institut fur Experimentalphysik, Technische Universitat Graz, 2000.

[28] P.K. Notz, O.A. Basaran, Dynamics and breakup of a contracting liquid filament, J. Fluid Mech. 512 (2004) 223–256, https://doi.org/10.1017/S0022112004009759.

[29] R. Pohl, C.W. Visser, G.W. Römer, D. Lohse, C. Sun, B. Huis in 'T Veld, Ejection regimes in picosecond laser-induced forward transfer of metals, Phys. Rev. Appl. 3 (2015) 1–9, https://doi.org/10.1103/PhysRevApplied. 3.024001.

[30] D.B. vanDam, C. LeClerc, Experimental study of the impact of an ink-jet printed droplet on a solid substrate, Phys. Fluids. 16 (2004) 3403–3414, https://doi.org/10.1063/1.1773551.